UNIVERSITÀ DEGLI STUDI DI PADOVA

Dipartimento di Fisica e Astronomia "Galileo Galilei"

Bachelor Degree in Physics

Final Dissertation

Testing the JUNO liquid scintillator response with test beam particles

Studio della risposta dello scintillatore liquido di JUNO con un fascio di particelle

Thesis supervisor

Prof. Alberto Garfagnini

Thesis co-supervisor

Dr. Beatrice Jelmini

Candidate

Elena Pasini

Academic Year 2023/2024

Abstract

The Jiangmen Underground Neutrino Observatory (JUNO) will be the largest liquid scintillator-based neutrino detector ever constructed. Thanks to its very large active mass (20 kton) and competitive performances (3% effective energy resolution at 1 MeV), it will be able to perform important measurements in neutrino physics. JUNO employs an organic liquid scintillator as the target for the neutrino interactions, and the main detection technique is to measure the light produced by de-excitation of the liquid scintillator. To validate the performances of the final liquid scintillator recipe that will be used in JUNO, a dedicated test beam measurement was set up at the Legnaro National Laboratories (INFN).
This thesis work focuses on the study of the response of the final JUNO liquid scintillator recipe to neutrons and gammas and aims at investigating its energy non linearities.

JUNO (Jiangmen Underground Neutrino Observatory) sarà il più grande rivelatore di neutrini a scintillatore liquido ad oggi mai costruito. Grazie alle sue grandi dimensioni (20 kton di massa attiva) e prestazioni all'avanguardia (3% di risoluzione in energia a 1 MeV), riuscirà ad effettuare importanti misure nell'ambito della fisica del neutrino. JUNO utilizza uno scinitllatore organico liquido come bersaglio per le interazioni dei neutrini. La principale tecnica di rivelazione in questa tipologia di detector consiste nel misurare la luce di scintillazione prodotta dalla diseccitazione delle molecole dei loro costituenti.
Al fine di valutare le prestazioni energetiche della miscela finale scelta per lo scintillatore liquido di JUNO, è stato ideato un apposito esperimento ai Laboratori Nazionali di Legnaro (INFN). Questo lavoro di tesi si incentra sull'analisi della risposta della miscela finale di JUNO all'interazione con gamma e neutroni e si propone come obiettivo quello di dare una stima degli effetti di non linearità nella sua risposta energetica.

Contents

Chapter 1

Introduction

This work focuses on the study of the scintillation response of the final cocktail of the JUNO liquid scintillator to neutrons and gammas. Sections 1.1 and 1.2 of this chapter provide an overview of the context of this work.
A dedicated experiment was set up at the Legnaro National Laboratories (LNL-INFN) by the JUNO group led by Prof. Hans Steiger (TUM). The measurements examined in this thesis were taken during the data acquisition campaign of December 2023.
A description of the experimental setup is given in Chapter 2. In Chapter 3, the calibration of the experimental setup is performed. Finally, in Chapter 4 the energy non-linearities in the response of the employed LS sample are analyzed.

1.1 The JUNO Experiment

The Jiangmen Underground Neutrino Observatory (JUNO) is a 20 kton multi-purpose Liquid Scintillator (LS) detector that aims at achieving several objectives in neutrino and astro-particle physics. JUNO was proposed with the determination of the neutrino mass ordering and the precise measurement of some of the oscillation parameters as its primary physics goals [1].
JUNO will detect electron antineutrinos produced by two nearby nuclear power plants via the inverse β-decay (IBD) reaction $\bar{\nu}_e + p \rightarrow n + e^+$. The IBD reaction proceeds as follows: an electron antineutrino ($\bar{\nu}_e$) interacts with a quasi-free proton of the 20 kton organic LS and creates a positron (e^+) and a neutron (n). The e^+ quickly deposits its energy and annihilates into two 511 keV photons, providing a prompt signal. The neutron scatters in the detector until thermalized and captured onto protons, with the release of a 2.2 MeV photon after ≈ 200 µs. The time coincidence between the prompt and delayed signals is employed to suppress background events [1].
In order to achieve its scientific goals, the relative energy resolution of JUNO is required to be $3\%/\sqrt{E(\text{MeV})}$. Thus, it's fundamental to maximize the scintillation light output of the LS. The optimal recipe for the JUNO LS was found to contain a mixture of Linear Alkyl Benzene (LAB) as a solvent, 2.5 g/L PPO (2,5-diphenyloxzole) as a fluor and 3 mg/L bis-MSB (p-bis-(o-methylstyryl)-benzene) for the wavelength shifter [2].
Energy non linearity of the LS poses a major challenge in JUNO, hence why a precise determination of this effect is required and is the topic of this work.

1.2 Liquid Scintillators and Ionization Quenching

When a charged particle passes through the LS, ionization energy loss is converted to scintillation light by de-excitation of LS molecules.
In case of charged particles with high energy losses per path length $\frac{dE}{dx}$, not all the deposited energy might be converted into scintillation light. The non linearity between the emitted scintillation light and the deposited energy is called **quenching effect**. Birks semi-empirical formula, eq. (1.1), describes this non-linear behavior. The differential scintillation response is given by [3]:

$$\frac{dL}{dx} = \frac{S \cdot \frac{dE}{dx}}{1 + kB \cdot \frac{dE}{dx}} \tag{1.1}$$

where $\frac{dE}{dx}$ is the particle stopping power, S is the scintillation efficiency and kB is the Birks factor. The visible energy in the detector (E_{vis}), which corresponds to the total amount of light emitted through scintillation, can be calculated as:

$$E_{vis} = \frac{L}{S} = \int_0^{E_{dep}} \frac{1}{1 + kB \cdot \frac{dE}{dx}(E)} dE \tag{1.2}$$

where L is the total light output obtained from the integration of eq.(1.1) and E_{dep} is the energy deposited by the particle in the detector.
The quenching effect manifests itself predominantly for heavy charged particles with lower momentum since they have higher stopping power values as can be inferred from Figure 1.1.

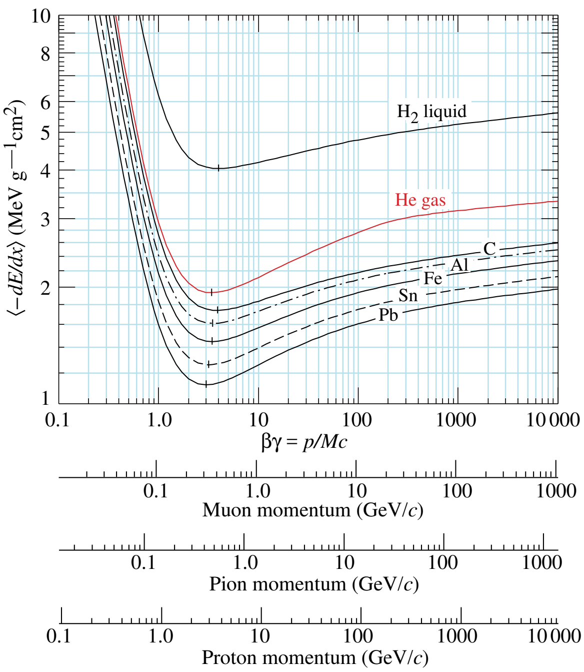

Figure 1.1: Mean mass stopping power for muons, pions and protons in three different mediums as a function of p/Mc. Figure taken from [4].

Neutron-induced proton recoil ionization quenching plays a significant role in several signal and background events in the JUNO experiment [5]; for example, fast neutrons of cosmogenic origin can mimic the IBD signature with a proton recoil as the prompt signal and a delayed neutron capture as the delayed signal. For this reason, it's important to have a good understanding of the LS response to neutron induced proton recoils.
Recent studies on this topic can be found in [6, 7].

Chapter 2

Experimental Apparatus

This section presents the apparatus that was used to perform the measurements with beam particles. Further details are available in [8, 9].

2.1 The INFN-LNL Setup

The measurements examined in this work were performed at the INFN Laboratori Nazionali di Legnaro (LNL).
The JUNO LS sample was placed in the beam-line of the CN Van-de-Graaf accelerator with the aim of examining its scintillation response to neutrons and gammas (γs). The experimental setup is shown in figure 2.1.

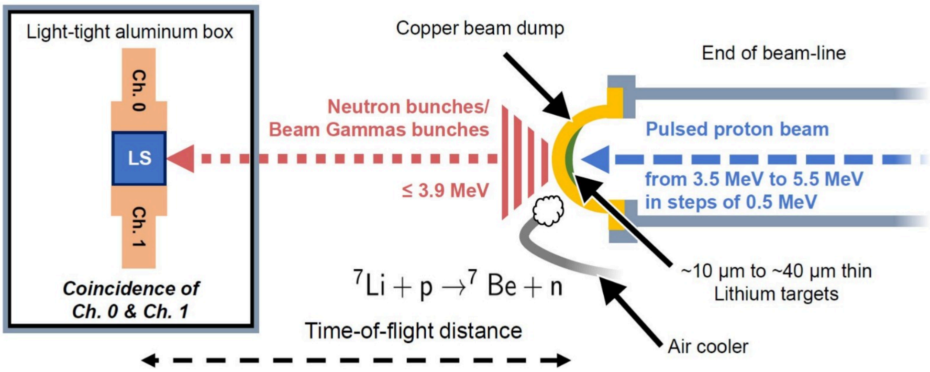

Figure 2.1: Experimental setup at INFN-LNL. The accelerated proton beam is directed onto a lithium target that subsequently emits neutrons with fixed energies and γs. The emitted particles travel a distance $L = 3.455 \pm 0.035$ m (time of flight distance) before reaching the LS detector. The LS in contained within a 3"x3" glass cell and placed into a light-tight mirrored aluminum dark box. The scintillation light emitted by the energy deposition of the particles in the LS is subsequently detected by two 3" photomultiplier tubes (PMTs). Figure taken from [8].

The CN accelerator was employed to accelerate a proton beam at five different energies (E_{beam}). The five E_{beam} energies ranged from 3.5 MeV to 5.5 MeV in steps of 0.5 MeV. The accelerated proton beam was then directed towards a ≈ 20 µm thick lithium target (enclosed in a copper shell to protect it from oxidation) in order to produce quasi-monoenergetic neutrons according to the nuclear reaction in eq. 2.1:

$$^7\mathrm{Li} + \mathrm{p} \rightarrow {}^7\mathrm{Be} + \mathrm{n}, \tag{2.1}$$

with $Q_{value} = 1.644$ MeV.
The energy of the neutrons E_n produced in the ^{7}Li(p,n)^{7}Be reaction can be calculated as:

$$E_n = E_{beam} - Q_{value} \tag{2.2}$$

These fast neutrons interact in the LS mainly through elastic scattering with its protons.
The energy deposited in the LS by the recoil proton is given by [10]:

$$E_{dep} \equiv E_{recoil} = E_n \frac{4m_p m_n}{(m_p + m_n)^2} \cos^2\theta \tag{2.3}$$

where E_n is the energy of the neutron and θ is the angle between the direction of the incoming neutron and the direction of the scattered proton in the laboratory frame.

The neutrons and γs emitted after the interaction of the beam protons on the Li/Cu target travel a time of flight distance L ≈ 3.455 m before reaching the LS. The scintillation light emitted by their energy deposition is detected by two PMTs connected to a triple coincidence circuit.
Figure 2.2 illustrates the structure of the employed circuit. Further details can be found in [8].

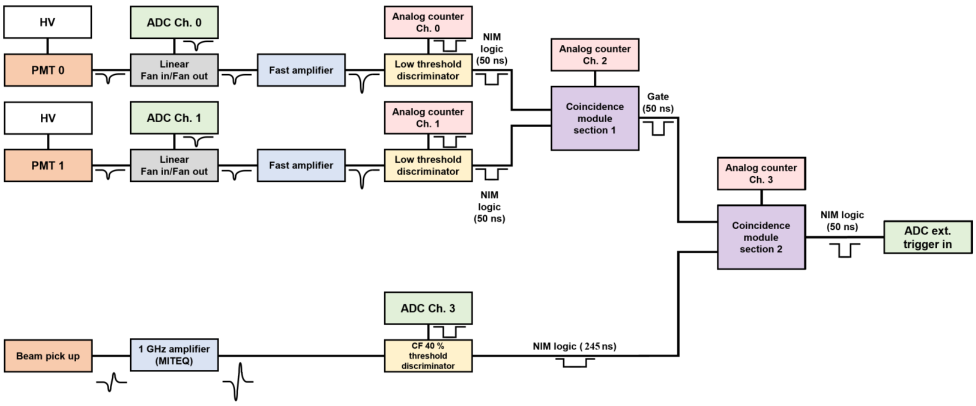

Figure 2.2: Triple coincidence circuit. Figure taken from [8].

The circuit is composed of two sub-circuits: the upper one is dedicated to the identification of the coincidence between the signals from the two PMTs; the bottom one is related to the beam start signal.
The triple coincidence circuit employs a Constant Fraction Discriminator (CFD) to provide precise time markings of the arrival of the pulses from the PMTs and the beam.
The CFD is a pulse shaping circuit. The input signal is delayed and inverted and a fraction of the original signal is added to it to form the Constant Fraction Timing signal, a bipolar pulse; its zero-crossing is then identified to create an output logic pulse that provides a time marker at the optimum fraction of the pulse height [11].
The time markings of the pulses from the PMTs and the beam are used to obtain the neutron time of flight (TOF), as described in sec. 4.2 .

Chapter 3

Energy Calibration

A fundamental preliminary step for the analysis of the beam data was the energy calibration of the detector.
The gamma emitting sources that had been chosen for this purpose were ^{22}**Na**, ^{133}**Ba** and ^{137}**Cs**. The setup described in sec. 2.1 had not been altered during the calibration measurements [9]. Given the low Z of the LS compound and its limited size, the main interaction process of photons in the LS is Compton scattering with its electrons. In this process, the recoil electron deposits its energy continuously in the LS up to a maximum energy, called Compton edge energy, E_{CE} . E_{CE} is calculated as follows:

$$E_{CE} \equiv E_e^{max} = \frac{E_\gamma^2}{2E_\gamma + m_e c^2} \tag{3.1}$$

where E_γ is the energy of the emitted photon and m_e is the mass of the electron.

In view of the above experimental facts and considering the limited energy resolution of the setup, we assume that the detector response function R is described by the complementary Gauss error function *Erfc* [8]:

$$R \propto Erfc\left(\frac{E - E_{CE}}{\sqrt{2}\sigma}\right) \tag{3.2}$$

3.1 Compton Edge Fitting

The raw data from the recorded pulses had been processed via the "`DataProcessor`" software [8] to reconstruct the relevant observables.
The integrated charge spectra of the ^{22}Na, ^{133}Ba and ^{137}Cs sources were each fitted with the complementary Gauss error function *Erfc* (eq. 3.3) in order to reconstruct their Compton Edge (CE) positions.

$$Erfc(x) = \frac{2A}{\pi} \int_{\frac{x-\mu}{\sigma}}^{\infty} e^{-t^2}\, dt + C \tag{3.3}$$

where μ corresponds to the reconstructed Compton edge position, σ is a parameter that accounts for the detector resolution, and A, C are constants [12].

The obtained fit values are presented in Table 3.1 along with the expected Compton edge energies of the gamma sources. Figure 3.1 shows an example of the fitting of eq. (3.3) to the second CE of the ^{22}Na calibration source. The fitted spectra of the other calibration sources can be found in appendix A.1.

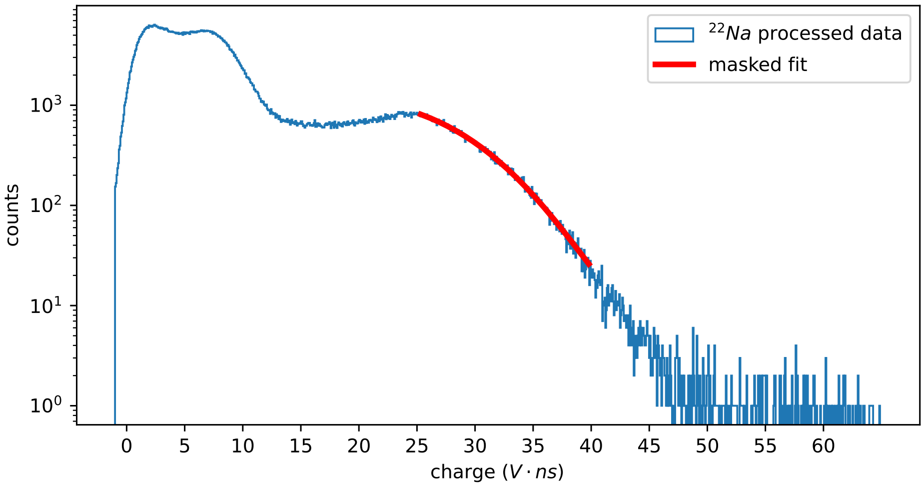

Figure 3.1: Fitting of the Compton edge of the integrated charge spectrum for the 1275 keV line of the ^{22}Na source. The region chosen for the fit includes a portion of the falling edge of the spectrum.

Table 3.1: Photopeak energies E_γ, theoretical Compton edges E_{CE}, and corresponding integrated charge values μ obtained from the fit with eq. (3.3) for all calibration sources.

Source	E_γ (keV)	E_{CE} (keV)	μ (V ns)
^{133}Ba	356	207	5.3092 ± 0.0002
^{137}Cs	662	477	12.294 ± 0.005
^{22}Na	511	341	8.899 ± 0.002
^{22}Na	1275	1062	27.6 ± 0.01

3.2 Calibration Parameters

Assuming a linear relation between the integrated charge and the deposited energy, the obtained CE positions are plotted against their theoretical values and a linear regression with the function in eq. (3.4) is performed as shown in fig. 3.2 (top).

$$f(E) = a \cdot E + b \tag{3.4}$$

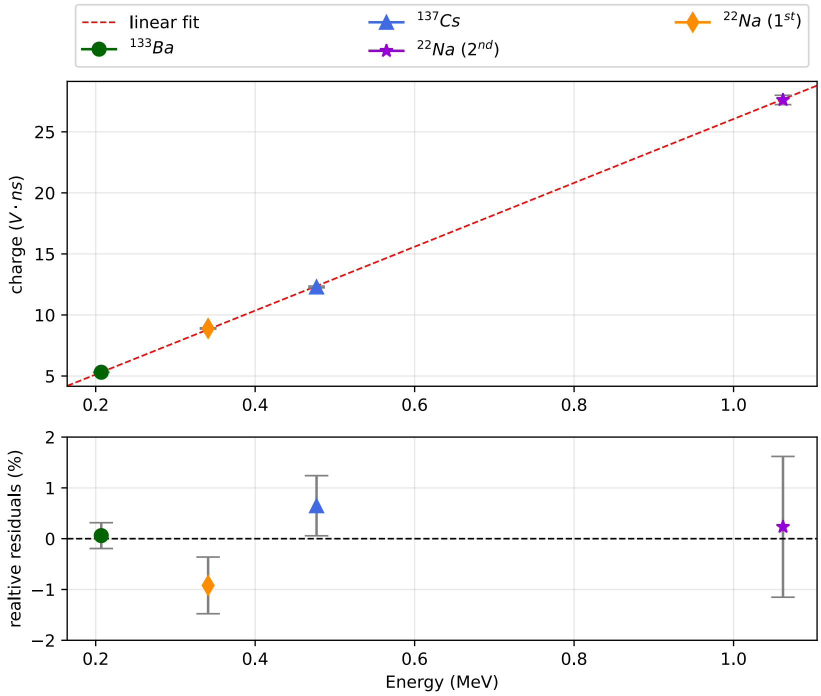

Figure 3.2: Plot of the energy-charge data points along with their fitted line (top) and relative residuals (bottom). The theoretical CE energies are assumed to have no uncertainties.

In order to calibrate the acquired integrated charge spectra, we are actually interested in the inverse relation described by eq. (3.5):

$$g(Q) = m \cdot Q + q \tag{3.5}$$

where Q is the integrated charge and m and q are the calibration parameters; m, q are retrieved from the best fit parameters a, b by reversing eq. (3.4).
Table 3.2 provides the values of a, b, m and q.

Table 3.2: Results of the fitting of the function $f(E) = a \cdot E + b$ to the calibration sources. The calibration parameters m, q are retrieved from a, b by the following relations: $m = \frac{1}{a}$, $q = -\frac{b}{a}$.

a $\left(\mathrm{V\,ns\,MeV^{-1}}\right)$	b (V ns)	m $\left(\mathrm{MeV\,ns^{-1}\,V^{-1}}\right)$	q (MeV)
26.2 ± 0.3	-0.10 ± 0.07	0.0382 ± 0.0004	0.004 ± 0.003

Figure 3.3 shows an example of a calibrated energy spectrum; the expected positions of the Compton edges are also shown.

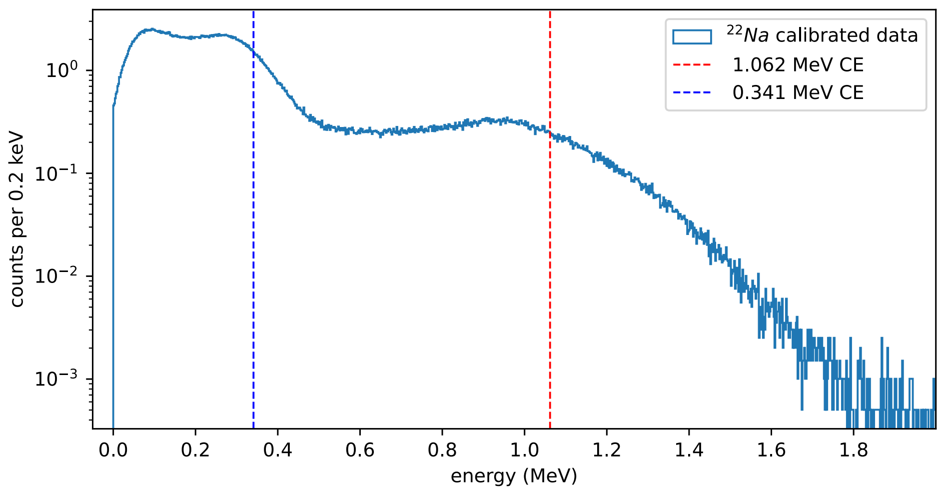

Figure 3.3: Calibrated visible energy spectrum for the ^{22}Na source. Two Compton edges are visible. The blue and red dashed lines represent the values of the expected CE energies for the 511 keV and 1275 keV lines, respectively.

Chapter 4

Beam Data Analysis

This chapter discusses the analysis of the scintillation response of the investigated LS sample to neutrons and gammas over five different energy values.
A detailed description of the experimental setup can be found in Chapter 2.

4.1 Datasets

The energy of the proton beam varied in the range of 3.5-5.5 MeV in steps of 0.5 MeV. For each beam energy, multiple runs were acquired. Table 4.1 provides a summary of the available data.

Table 4.1: Brief summary of the number of runs and their size for each beam energy. Test runs were discarded from the analysis.

Beam energy (MeV)	No. of runs	Tot. No. of events
3.5	9	12×10^6
4	8	12.6×10^6
4.5	13	26×10^6
5	10	26×10^6
5.5	21	48×10^6

The raw data from these runs were first processed using the "`DataProcessor`" software provided by the TUM group [8] and later combined together to form energy specific datasets.
The quantities of interest extracted from the processed data were the integrated charge ("`integral`") and the Constant Fraction Time ("`CFT`") of the pulses of the PMTs and the beam (see sec. 2.1).

In order to reconstruct the visible energy in the LS, the integrated charge is calibrated using the parameters found in table 3.2. The visible energy includes contributions from gammas and neutrons, as they both deposited their energy in the LS. Figure 4.1 shows the calibrated visible energy spectra.

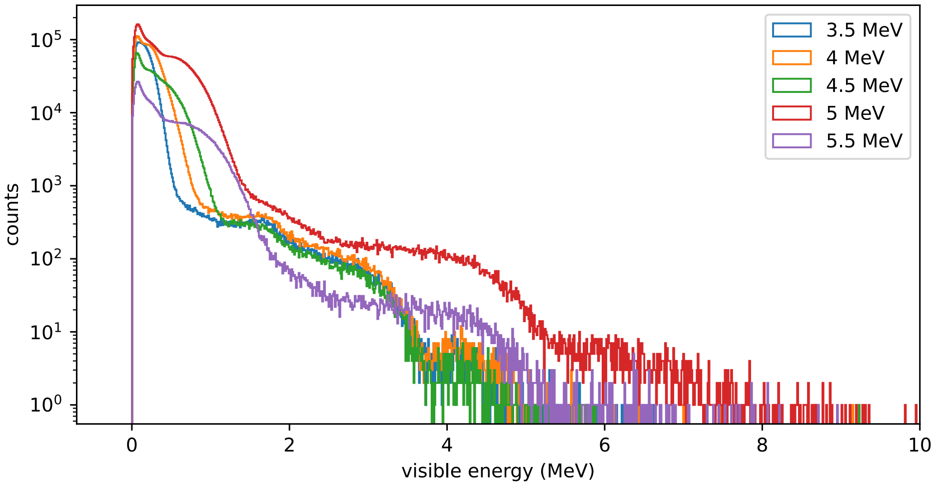

Figure 4.1: Calibrated visible energy spectra for the five beam energies. The visible energy includes contributions from both gammas and neutrons.

4.1.1 Quality Checks on the Time of Flight

The Time Of Flight (TOF) is calculated as

$$\mathrm{TOF} = \mathrm{CFT}_{PMT} - \mathrm{CFT}_{beam} \tag{4.1}$$

where CFT_{PMT} and CFT_{beam} are the time markings of the logical signals from the PMT coincidence gate and the beam, respectively (see sec. 2.1).
In order to check for possible faulty data, a TOF histogram was created for each run. Subsequently, TOF histograms attributed to the same energy dataset were visualized together in the same graph.
Each histogram shows a distribution with two peaks: the first peak is associated to gamma events, the second to neutrons, as shown in fig. 4.2.

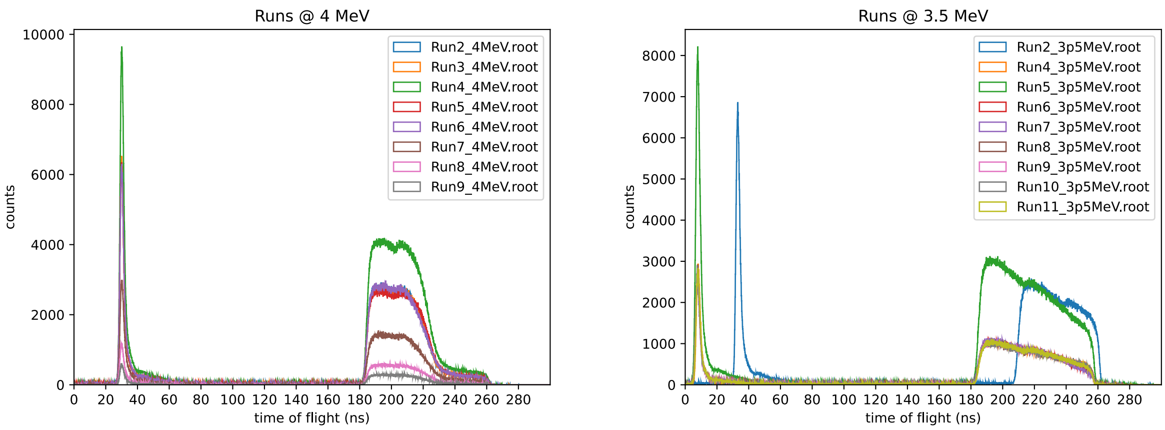

Figure 4.2: Left: TOF histograms for the 4 MeV dataset. All gamma peaks are aligned. Right: TOF histograms for the 3.5 MeV dataset. The "Run2" distribution is shifted towards higher values if compared to the others.

For the 3.5 MeV dataset, shown on the right of fig. 4.2, "Run2" had to be shifted in order to align its gamma flash to the others'. This discrepancy was attributed to a different experimental setting for that specific run. No other anomalies were observed.

After correcting for some minor inconsistencies in the data acquisition, the run-dependent TOF datasets were merged together to form five energy specific datasets.
The five uncalibrated TOF histograms are presented in Figure 4.3.

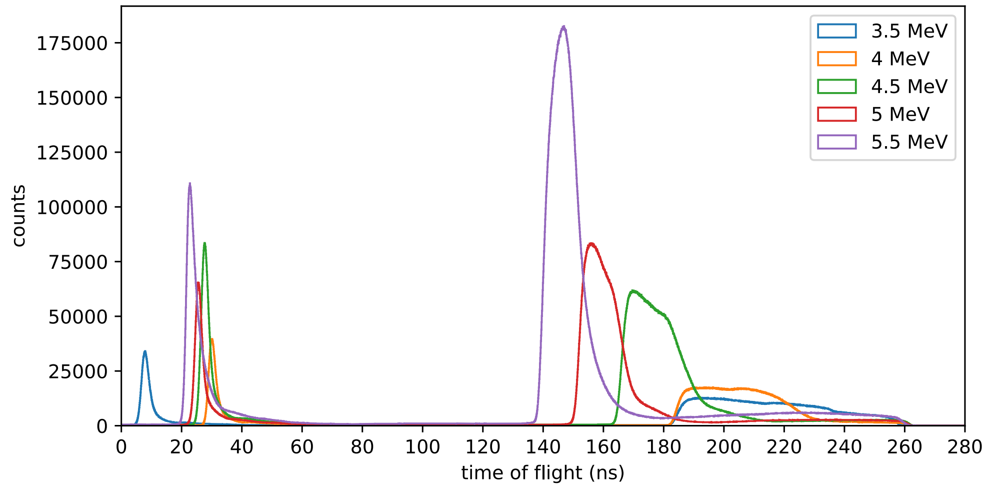

Figure 4.3: Uncalibrated TOF histograms for the five beam energies. Neutron and gamma peaks are visible.

As can be noticed from fig. 4.3, the γ peaks are found at different timings for the five beam energies. For a proper analysis, the histograms had to be calibrated. Their distributions were shifted in order to make the gamma peak position overlap with the expected timing $t_\gamma = 12 \pm 1$ ns. Figure 4.4 shows the calibrated TOF histograms.
The expected timing t_γ was computed as $t_\gamma = \frac{L}{c}$, where c is the speed of light and $L = 3.455 \pm 0.035$ m was deducted from the experimental settings. The actual value of the t_γ chosen for the timing calibration has no relevance in the data analysis; its only purpose is to give a timing reference for all the TOF spectra that will be subsequently employed to separate the neutron events from the gamma's.

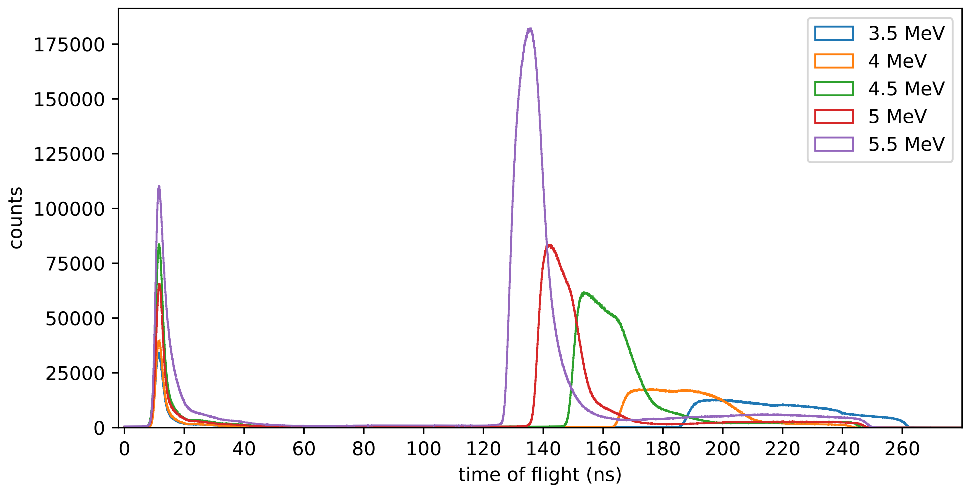

Figure 4.4: Calibrated TOF histograms for the five beam energies. Neutron and gamma peaks are visible. The distributions were shifted so that the γ peaks would all line up to their expected value of ≈ 12 ns.

4.2 Data Selection

As previously mentioned in ch. 2, the ^{7}Li(p,n)^{7}Be reaction produces *quasi*-monoenergetic neutrons. The prefix *quasi* derives from the fact that neutrons can lose part of their energy in the Li target before reaching the LS [8]. Hence, their energy spectrum forms a continuous distribution. Since we are interested in neutrons with a monochromatic energy spectrum for the purposes of the analysis in sec. 4.3, a data selection based on the their time of flight is performed.

The TOF cut consists in the following procedure. The front tail of the neutron peak is fitted to a Gaussian distribution and its mean μ and standard deviation σ are retrieved. Subsequently, the interval that represents the most energetic neutrons is determined as $[\mu - 2\sigma, \mu]$, where the left bound defines the upper limit for the fastest neutrons.
Figure 4.5 shows the Gaussian fits and TOF cut regions for the 3.5 MeV and 5.5 MeV datasets. The results for the other datasets are reported in appendix A.2.

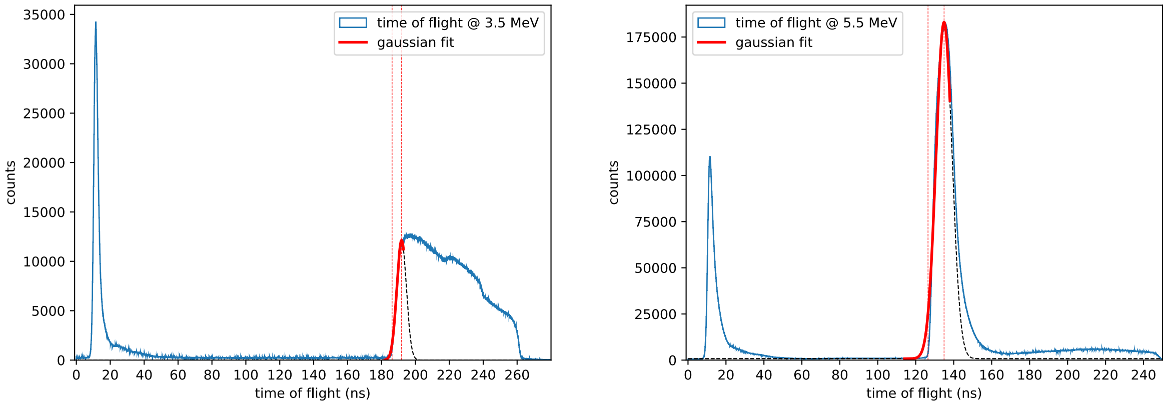

Figure 4.5: Examples of gaussian fits of the front tails of the neutron peaks for two different beam energies. For the 3.5 MeV dataset, the neutron peak is more widened. The red dashed vertical lines depict the lower and upper bounds of the TOF cut.

The TOF cut interval was then employed to obtain the visible energy (E_{vis}) associated to the most energetic neutrons. More specifically, the `integral` dataset was sliced by taking the same indices provided by the TOF cut.
Figure 4.6 provides the E_{vis} spectra for the five beam energies.

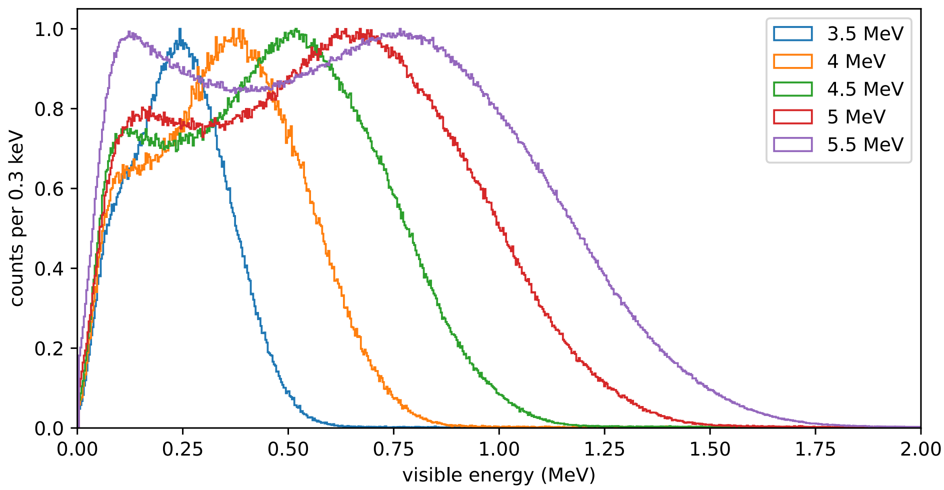

Figure 4.6: Visible energy spectra after applying the neutron events cut. The spectra have been normalized by dividing their counts by the maximum bin height. A distribution with two separate peaks can be noticed for the higher beam energies. On the other hand, the distribution is more spread out at lower energies.

4.3 Quenching Effect Estimation

As previously discussed in Chapter 2, the fast neutrons produced in the ^{7}Li(p,n)^{7}Be reaction deposit their energy predominantly through elastic scattering with the protons of the LS.
Only events corresponding to their maximum energy deposition are examined for the quenching effect evaluation.
These events are compatible with head-on collisions ($\theta = 0$) between the neutron and the proton. In this case, eq. (2.3) can be rewritten as:

$$E_{dep}^{max} = E_n \frac{4m_p m_n}{(m_p + m_n)^2} \tag{4.2}$$

Furthermore, with the approximation $m_n \approx m_p$, we can write:

$$E_{dep}^{max} = E_n = E_{beam} - Q_{value} \tag{4.3}$$

The analysis of the non-linearity of the LS response is based on the calculation of the ionization Quenching Factors (QF), defined in (4.4) as the ratio between the visible and deposited energy by neutron-induced proton recoils in the detector.

$$QF = \frac{E_{vis}^{max}}{E_{dep}^{max}} \tag{4.4}$$

where E_{vis}^{max} corresponds to the visible energy associated to the maximum energy deposited by a neutron, E_{dep}^{max}, evaluated as in eq. (4.3).

For a proper quantitative analysis of the quenching effect, a Monte Carlo simulation of the experimental setup should have been employed for a precise estimation of the E_{vis}^{max} energy.
The subsequent analysis is therefore carried out under the simplifying assumption that E_{vis}^{max} can be found in the region of the rightmost peak of the visible energy spectra.

4.3.1 Fitting with the Landau-Gaussian Function

The second peak of each visible energy spectra is fitted to the the convoluted Landau and Gaussian function in order to estimate the value of E_{vis}^{max}.
The Landau distribution describes the fluctuations in energy loss of charged particles in matter. Its analytic expression is given in eq. (4.5) [12]:

$$L(E; MPV, c) = \frac{1}{\pi c} \int_0^\infty e^{-t} \cos\left(t\left(\frac{E - MPV}{c}\right) + \frac{2t}{\pi} \log\left(\frac{t}{c}\right)\right) dt \tag{4.5}$$

where MPV is a location parameter corresponding to the most probable value of the distribution and c is a scale parameter. This function is then convoluted with a Gaussian distribution to take into account the finite energy resolution of the detector.
Figure 4.7 shows a fitting example for the 5.5 MeV dataset. The complete analysis is found in appendix A.3. The obtained MPV values of the five spectra, which represent an estimation of the E_{vis}^{max} positions, are presented in table 4.2 along with their beam energies; the value of the deposited energy E_{dep}^{max} is also reported.

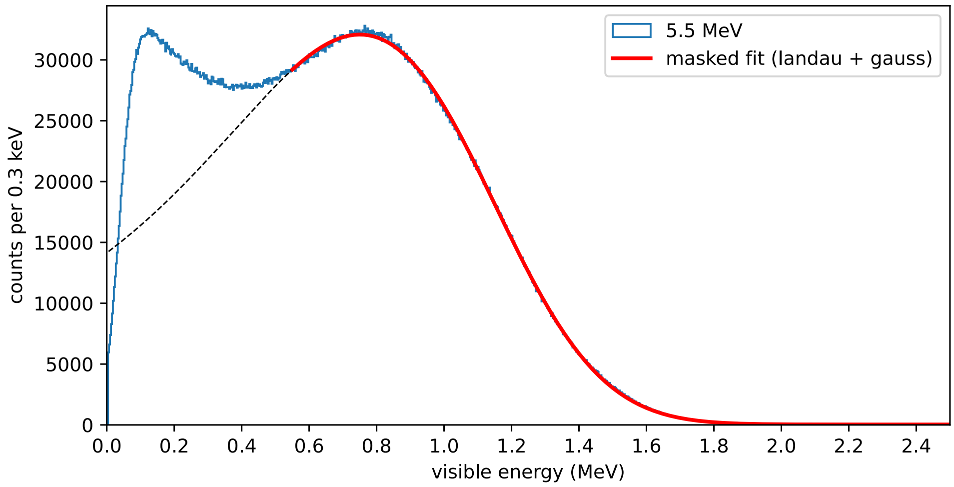

Figure 4.7: Fitting of the E_{vis} spectrum at 5.5 MeV with the convoluted Landau and Gaussian function. The region to fit was chosen as to include the second peak and falling edge of the spectrum.

Table 4.2: MPV values obtained from the fitting of the convoluted Landau and Gaussian function to the experimental visible energy spectra for each beam energy. E_{dep}^{max} was calculated as $E_{dep}^{max} = E_{beam} - Q_{value}$.

E_{beam} (MeV)	MPV (MeV)	E_{dep}^{max} (MeV)
3.5	0.25	1.856
4	0.38	2.356
4.5	0.51	2.856
5	0.65	3.356
5.5	0.75	3.856

4.3.2 Quenching Factors Plot

Quenching factors are evaluated by taking the previously obtained MPV values (Table 4.2) as the value of E_{vis}^{max}.
The neutron-induced proton recoil quenching effect can be visualized by plotting the quenching factors estimated as in eq. (4.4) against the energy deposited by neutrons E_{dep}^{max}. The plot is shown in Figure 4.8.

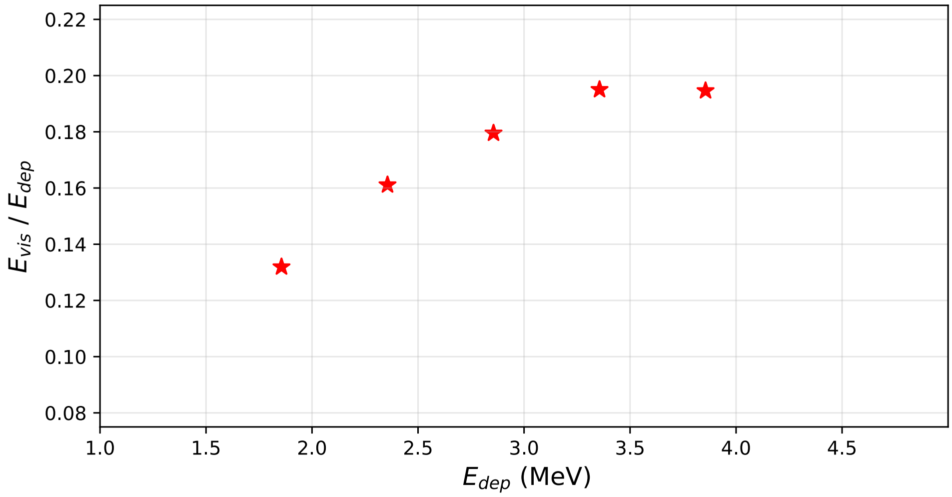

Figure 4.8: Plot of the quenching factors in function of the deposited energy. The data points show a non linear trend.

The QF values must be interpreted with caution because of the uncertainty of the location of E_{vis}^{max} due to the simplifying assumption that the rightmost peak corresponds to the case in which all the neutron energy is transferred to the proton, so that $E_{dep}^{max} = E_n$.

Nevertheless, we can say that overall the experimental data-points suggest a non-linear relation that could be further proved to be described by the usual ionization quenching models found in literature (*e.g.* Birks' model [3]).
Further work, which should take into account a Monte Carlo simulation of the experimental setup, is required for a precise estimation of the quenching factors.

Chapter 5

Conclusions

The aim of this thesis was to assess the response of the final JUNO liquid scintillator recipe to neutrons and gammas. A dedicated test beam measurement was set up at the INFN Legnaro National Laboratories in order to investigate the neutron-induced proton recoil quenching effect in the 3.5-5.5 MeV energy range.

The first part of the analysis was centered on the energy calibration of the experimental setup. Subsequently, after carrying out some necessary quality checks on the acquired measurements, the Time of Flight cut method allowed for the separation of neutrons from gammas, for the selection of the most energetic neutrons, and the reconstruction of their visible energy spectra. Afterwards, the visible energy associated to the maximum energy deposited by a neutron was reconstructed and employed to finally evaluate the ionization Quenching Factors (QF).
The obtained QF values must be interpreted with caution due to the simplifying assumptions that had been made in order to carry out the analysis of the visible energy spectra.
Nevertheless, the results of this analysis suggests the presence of a non-linear response that could be further proved to be described by the ionization quenching models found in literature.
For a more precise estimation of the quenching factors, further work should take into account a Monte Carlo simulation of the experimental setup.

Appendix A

Additional figures

A.1 Compton Edges

Figures A.1 and A.2 show the fitting with the *Erfc* of the Compton edges of the uncalibrated energy spectra of the ^{133}Ba and ^{137}Cs and the ^{22}Na sources.

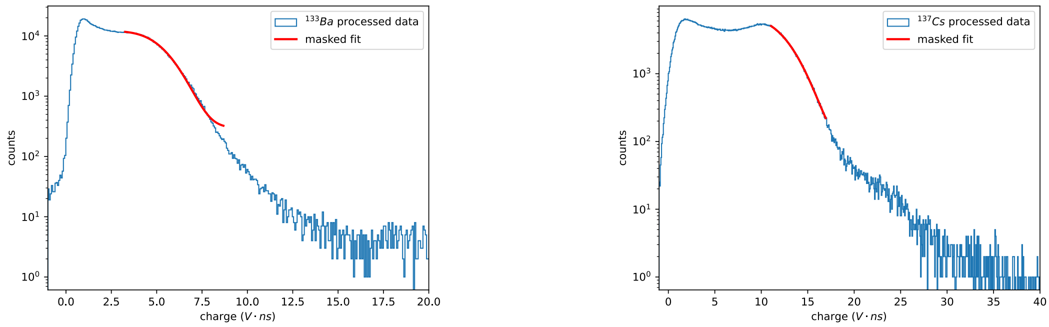

Figure A.1: Left: ^{133}Ba CE fit. Right: ^{137}Cs CE fit.

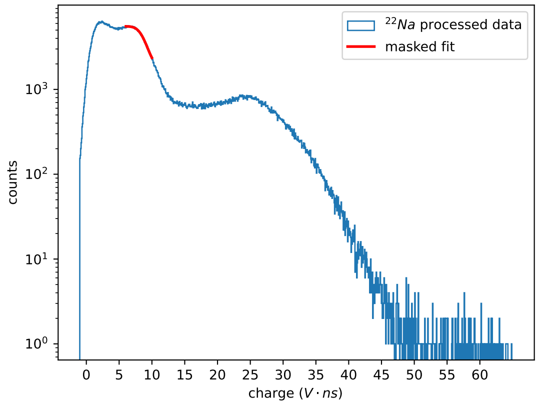

Figure A.2: ^{22}Na first CE fit.

A.2 Time of Flight Cut

Figures A.3 and A.4 show the gaussian fits of the front tails of the neutron peaks and TOF cut intervals for the 4 MeV, 4.5 MeV and 5 MeV datasets.

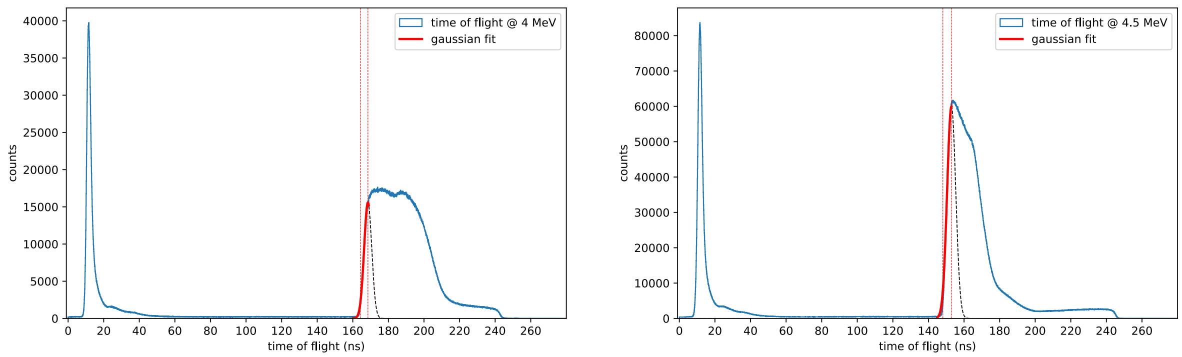

Figure A.3: Left: Gaussian fit and TOF interval for the 4 MeV dataset. Right: Gaussian fit and TOF interval for the 4.5 MeV dataset.

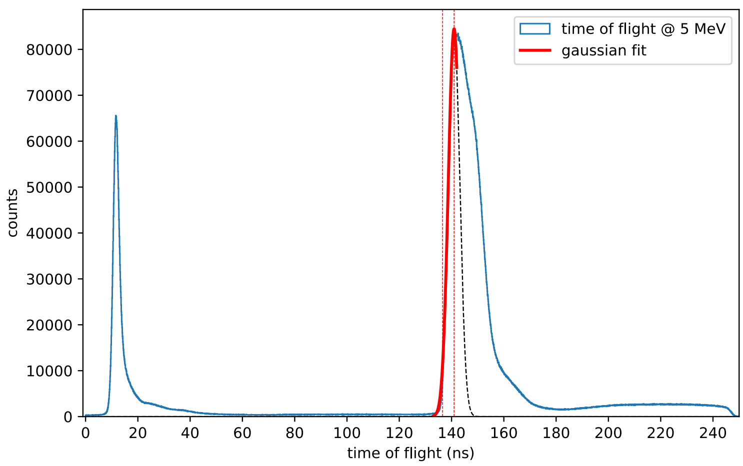

Figure A.4: Gaussian fit and TOF interval for the 5 MeV dataset.

A.3 Fitting with the Convoluted Landau and Gaussian Function

Figure A.5 shows the fits with the convoluted Landau and Gaussian function of the falling edges of the E_{vis} spectra for the 3.5 MeV, 4 MeV, 4.5 MeV and 5 MeV datasets.

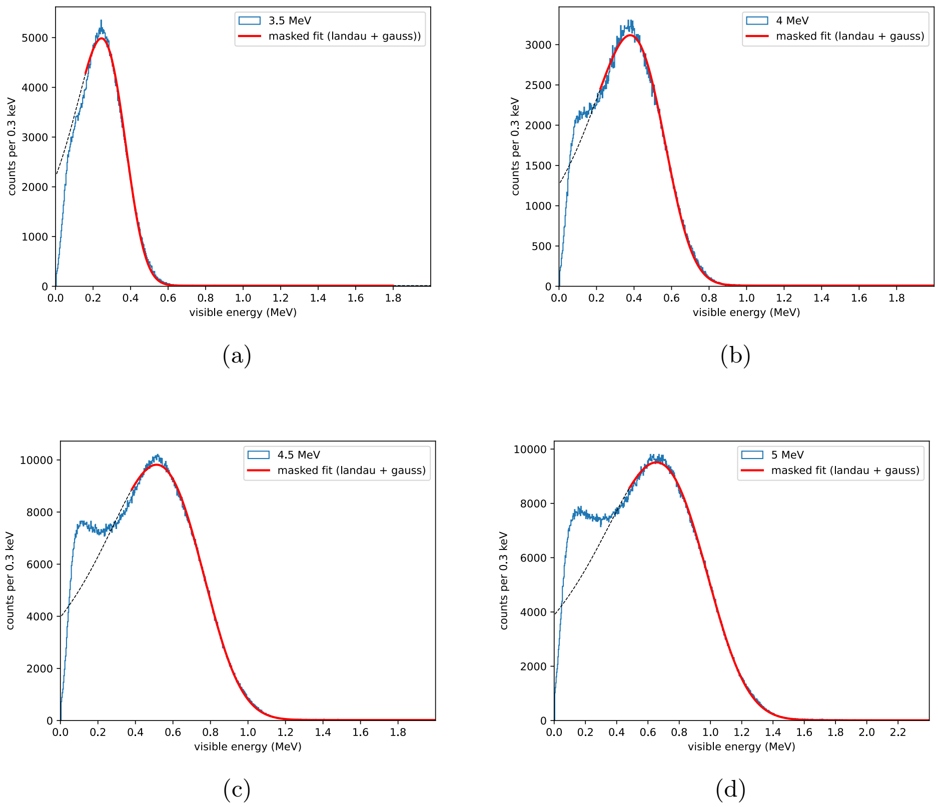

Figure A.5: (a) 3.5 MeV (b) 4 MeV (c) 4.5 MeV (d) 5 MeV

Bibliography

[1] Fengpeng An et al. “Neutrino Physics with JUNO”. In: *J. Phys. G* 43.3 (2016), p. 030401. DOI: 10.1088/0954-3899/43/3/030401. arXiv: 1507.05613 [physics.ins-det].

[2] Angel Abusleme et al. “JUNO physics and detector”. In: *Prog. Part. Nucl. Phys.* 123 (2022), p. 103927. DOI: 10.1016/j.ppnp.2021.103927. arXiv: 2104.02565 [hep-ex].

[3] J.B. Birks. “The Theory and Practice of Scintillation Counting”. In: International Series of Monographs in Electronics and Instrumentation. Pergamon, 1964, pp. 185–234. ISBN: 978-0-08-010472-0. DOI: https://doi.org/10.1016/B978-0-08-010472-0.50011-2. URL: https://www.sciencedirect.com/science/article/pii/B9780080104720500112.

[4] R. L. Workman et al. “Review of Particle Physics”. In: *Progress of Theoretical and Experimental Physics* 2022.8 (Aug. 2022), p. 083C01. DOI: 10.1093/ptep/ptac097. URL: https://doi.org/10.1093/ptep/ptac097.

[5] Zelimir Djurcic et al. “JUNO Conceptual Design Report”. In: (Aug. 2015). arXiv: 1508.07166 [physics.ins-det].

[6] Hans Th. J. Steiger et al. “Development, Characterization and Production of a novel Water-based Liquid Scintillator based on the Surfactant TRITON X-100”. In: (May 2024). DOI: https://doi.org/10.48550/arXiv.2405.01100. arXiv: 2405.05743 [hep-ex].

[7] Hans Th. J. Steiger et al. “Development of a Bi-solvent Liquid Scintillator with Slow Light Emission”. In: (May 2024). DOI: https://doi.org/10.48550/arXiv.2405.05743. arXiv: 2405.01100 [physics.ins-det].

[8] David Jan Dörflinger. “High Precision Measurement of Proton Recoil Quenching Factors in Liquid Scintillators”. Master thesis. Technische Universität München, 2023.

[9] Benedetta Rasera. “Calibrazione in energia dell’apparato su fascio per lo studio dello scintillatore liquido di JUNO”. Available at https://hdl.handle.net/20.500.12608/64683. Bachelor thesis. University of Padova, 2023.

[10] Stefaan Tavernier. *Experimental Techniques in Nuclear and Particle Physics*. 1st ed. Springer Berlin, Heidelberg, 2010. DOI: 10.1007/978-3-642-00829-0.

[11] ORTEC-AMETEK. *Fast-Timing Discriminator Introduction*. URL: https://www.ortec-online.com/-/media/ametekortec/other/fast-timing-discriminator-introduction.pdf.

[12] Riccardo Callegari. “Characterization and tests of 39 channels of the JUNO large PMT electronics”. Available at https://hdl.handle.net/20.500.12608/22810. Master thesis. University of Padova, 2020.